

High-performance Biopolymer Cryogels for Transient Sensing Ecology-drones

Fabian Wiesemüller¹, Severin Meyer¹, Yijie Hu¹, Dominik Bachmann¹, Annapaola Parrilli¹, Gustav Nyström¹, and Mirko Kovac¹

¹Affiliation not available

January 30, 2023

Abstract

Aerial robots can autonomously collect temporal and spatial high-resolution environmental data. This data can then be utilized to develop mathematical ecology models to understand the impact of climate change on our habitat. In case of the drone's malfunction the incorporated materials can threaten vulnerable environments. The recent introduction of transient robotics has enabled the development of biodegradable, environmental sensing drones capable of degrading in their environment. However, manufacturing methods for environmental sensing transient drones are rarely discussed. In this work, we highlight a manufacturing framework and material selection process featuring biopolymer-based, high-strength composite cryogels and printed carbon-based electronics for transient drones. We found that gelatin and cellulose based cryogels mechanically outperform other biopolymer composites while having a homogeneous micro-structure and high stiffness-to-weight ratio. The selected materials are used to manufacture a flying-wing air-frame, while the incorporated sensing skin is capable of measuring the elevons' deflection angles as well as ambient temperature. Our results demonstrate how gelatin-cellulose cryogels can be used to manufacture lightweight transient drones while printing carbon conductive electronics is a viable method for designing sustainable, integrated sensors. The proposed methods can be used to guide the development of lightweight and rapidly degrading robots, featuring eco-friendly sensing capabilities.

Corresponding author(s) Email: fabian.wiesemuller@empa.ch, mirko.kovac@empa.ch

ToC Figure

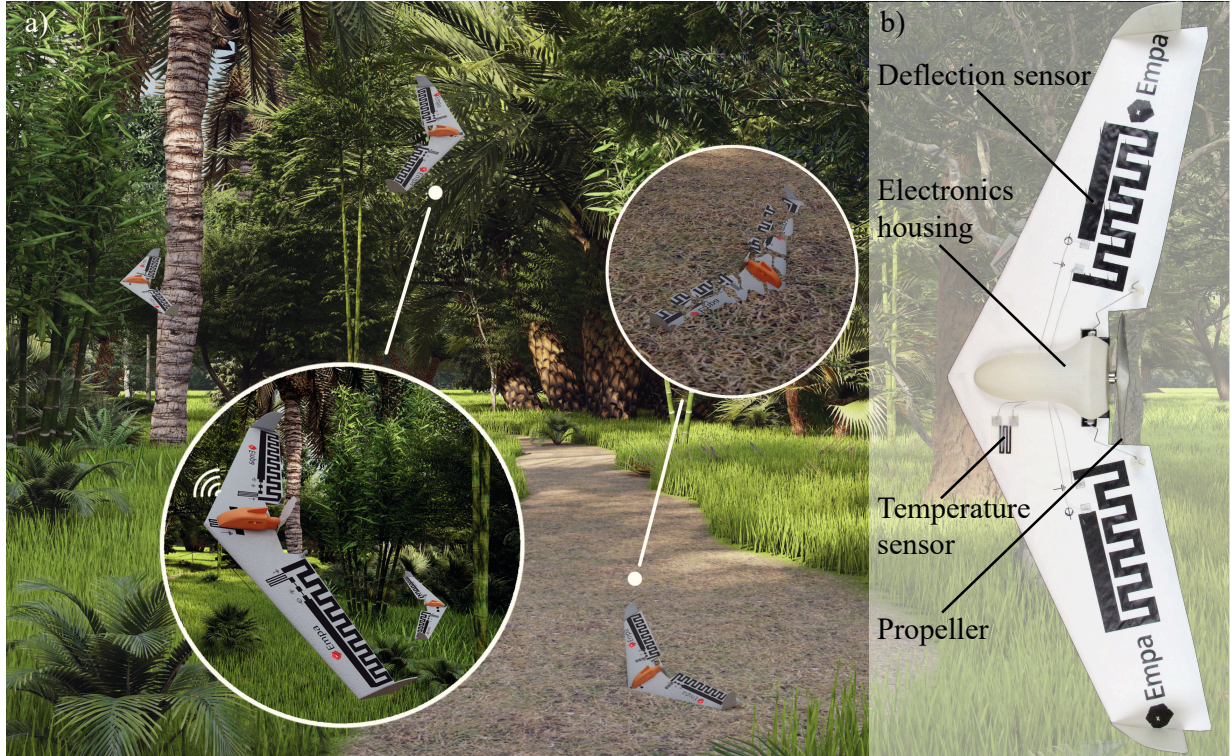


Figure 1: **ToC Figure.** Transient robots are biodegradable tools towards sustainable environmental monitoring in remote locations. In this work we propose manufacturing techniques to fabricate aerial robots from non-fossil, high-performance and lightweight biopolymer composite cryogels. By incorporating ink-jet printed carbon-conductive sensors, we can add proprioceptive and exteroceptive sensing capabilities and demonstrate the aerial robots data transmission as well as flightworthiness.

Introduction

In the changing environment, the world's natural forests provide a carbon sink that absorbs approximately two billion tonnes of CO_2 per year (Cavicchioli et al., 2019; FAO and UNEP, 2020). To further understand the forest's role and develop conservation strategies, more sophisticated energy balance models need to be developed that require a deeper understanding of various ecological mechanisms (Bauerle et al., 2009). Research activities need to focus on understanding changes in the vegetative phenology and the ecosystem energy or mass exchanges, that influence the ecosystem carbon production and productivity levels (Tymen et al., 2017; Naumburg and Ellsworth, 2000; Mo et al., 2009).

Further aspects need to be studied for estimating CO_2 budgets (Rödiger et al., 2018) and guide policymakers and environmentalists towards efficient strategies for optimizing carbon sequestration in forests (Ontl et al., 2020). For developing those models high temporal and spatial resolution environmental data is needed. This requires time-consuming, complex and expensive methods for manually distributing build-to-last sensing devices with human workers (Figueiredo et al., 2009). These sensing devices still propose a threat to the environment in which they are deployed in, as they are non-degradable and potentially toxic. Robotic platforms can be utilized to automatize data sampling while reducing risks and costs (Debruyne et al., 2020; Farinha et al., 2020). If the drone's control is lost, its structure and active components can pollute and harm the environment, targeted for monitoring. Recovery of this e-waste must then be guaranteed due to the potentially toxic nature of the materials utilized. This might be difficult to do, for hard-to-reach

and sensitive, environments. Therefore, their capabilities for autonomous environmental sensing of sensitive environments are limited.

To enable autonomous, robotic and eco-friendly environmental monitoring, transient robotic devices need to be manufactured purely from biodegradable and non-fossil-based materials (Wiesemüller et al., 2022). These transient drones (Wiesemüller et al., 2022, 2021; Sethi et al., 2022) are designed for collecting, storing and transmitting environmental data, by reaching difficult to access locations through flight. Due to the biodegradability of their active and passive components, these systems do not need to be recovered and can be left for degradation, where nutritional sources contained in their components are directly fed back into the biomass energy cycle. This eco-friendly approach to joint material and system development (Miriye and Kovač, 2020) for environmental monitoring can be a viable alternative to traditional robotic systems designed for monitoring and manipulating the environment. **Figure 2** shows a conceptual illustration of the herein proposed transient drone deployed in a tropical environment.

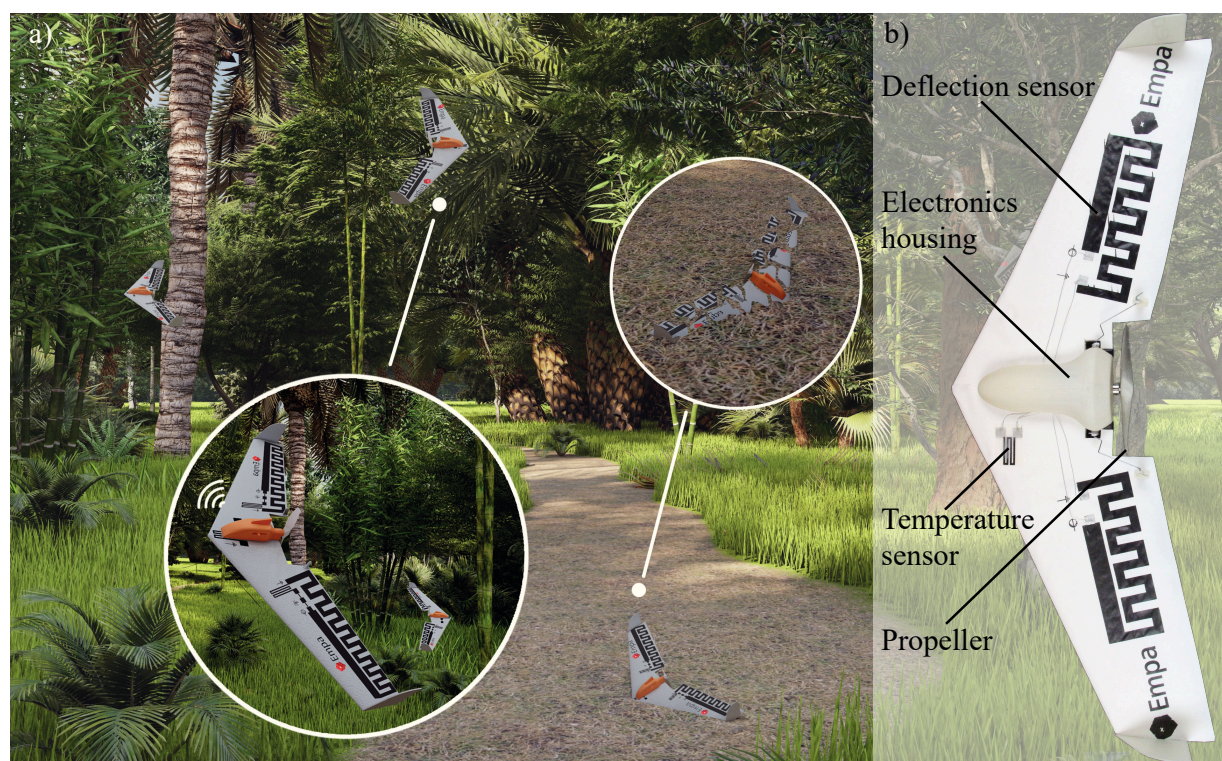


Figure 2: Developed transient drone for environmental monitoring. **a)** Conceptual illustration of the transient drone in a tropical environment. After the collection and transmission of environmental data, the drone crashes and the structures degrade. Only the electronics compartment painted in high-visibility colors remains and needs to be picked up by a field worker. **b)** Photograph of the final transient prototype indicating the main components.

To develop light-weight, but structurally high-performant transient drones, materials need to be developed that feature superior mechanical properties, inherent sustainability and biodegradability. Cellulose is a natural biopolymer composed of β -(1-4)-linked d-glucose units, with an annual synthesis of 75 billion tons (Ahankari et al., 2021), which makes it the most abundant polymer on earth. Its superior mechanical properties, inherent biodegradability as well as the possibility for functionalization (Kim et al., 2006; Li et al., 2021) makes it an ideal candidate for designing systems that can combine structural integrity, sensing capabilities and maintain eco-friendliness. For manufacturing a structurally efficient flying drone, the specific

stiffness, as well as the specific strength of the structure, need to be maximized. Since the bulk densities of cellulose and other biopolymers are too high, they do not qualify for a lightweight unmanned aerial drone. Cryogels or aerogels are light-weight material systems with good mechanical properties, featuring a porosity higher than 95 % and 99 % (Sehaqui et al., 2010) respectively. Cryogels are prepared through the lyophilization of frozen gels, while aerogels generally are prepared through supercritical drying (Zhao et al., 2018). Considering cellulose’s low cost, wide availability, and biodegradability, it is an ideal raw material for cryogel or aerogel preparation. To achieve a larger surface area as well as better mechanical properties, the cellulose is fibrillated, resulting in micro-fibrillated cellulose (MFC) - a three-dimensional network of microfibrils. Nevertheless, most cellulose-based foams show low mechanical strength, which is fatal for withstanding dynamic forces acting on the structure in-flight (Garemark et al., 2020; Buchtová et al., 2019; Kobayashi et al., 2014). The most effective way to improve the mechanical strength of cellulose-based foams is to enhance their networks by introducing polymers or nanofillers. For example, Fu et al. interconnected cellulose/boron nitride nanosheet skeletons with epichlorohydrin and polyethylene glycol via self-assembly, vacuum impregnation, and cold compressing and displayed a compressive strength of 3.03 MPa (Lei et al., 2019). Liu et al. prepared a ternary material system based on polyvinyl alcohol, montmorillonite clay platelets, and cellulose nanofibrils with a yield strength of 250 kPa and 95 % porosity. In situ chemical cross-linking using borax dramatically changed the cellular structure and improved its strength to almost 900 kPa (Liu et al., 2017). However, these methods usually contain toxic as well as fossil materials and complex preparation processes.

In this work, we introduce gelatin to form a cross-linked network with MFC to manufacture high-strength environmentally friendly structures, while comparing it to starch and agar MFC composites. Gelatin is a collection of peptides and proteins produced by partial hydrolysis of collagen extracted from the skin, bones, and connective tissues of animals. It can form cross-linked networks through sol-gel process. Via the composition of gelatin and MFC, the cross-linked porous structure can effectively transfer stress, leading to a high-strength cryogel with a strength of up to 542 kPa and a modulus of 12000 kPa. The developed material systems are utilized to manufacture the lightweight and biodegradable air-frame of a transient drone and combined with eco-friendly sensors, enabling proprioceptive and exteroceptive monitoring capabilities. For realizing full functionality traditional electronics were incorporated into an electronics housing, prohibiting the contamination of the environment with toxic components.

Fabrication

In this section, the manufacturing methods for generating the lightweight structures as well as the sensing skin of the proposed transient drone concept are presented. The foams were manufactured through lyophilization of MFC and biopolymer solutions or suspensions respectively. The sensing skin was prepared from carbon conductive ink printed on low-roughness cellulose paper using inkjet printing.

Material development

For the preparation of all cryogel composites, MFC was used and mixed with starch, agar and gelatin respectively. The manufacturing and characterization of the used MFC were performed according to our previous work (Josset et al., 2014, 2017; Antonini et al., 2019). As a summary, an ultra-fine friction grinder Supermass-colloider (MKZA10-20 J CE, Masuko Sangyo Co., Ltd., Kawaguchi/Saitama, Japan) with a grinding energy input of 9 kWh/kg (referred to dry MFC content) was used to ground aqueous Eucalyptus pulp suspension at an initial concentration of 2 wt%. To reach a solid content of about 11.6 wt% the MFC suspension was dewatered with a sieve under pressure. Lignin and hemicellulose were removed by the producer through bleaching the slurry. No chemical treatment (i.e., non-oxidized) was performed on the cellulose pulp before mechanical disintegration. For investigating the structural performance of different material combinations, a sweep over various weight contents ranging from 1% to 8% total solid content was performed. The biopolymers starch, agar and gelatin were mixed at a 1:1 weight content ratio with MFC. For

comparison, cryogels were prepared from the plain biopolymers MFC, starch, agar and gelatin. An overview of all the material combinations investigated, their respective cryogel mass ratios and the total, as well as the individual solid contents in the aqueous slurry, are given in Table 1 in section 1.3.1 in the supporting information.

All the cryogels were prepared following the same manufacturing steps. Varying amounts of MFC at 11.6 wt% were filled into a beaker and diluted to the required weight-content using deionized water. After closing the beaker using a glass plate, the MFC was homogenized using a magnetic stirrer and heated to 40 °C. In parallel, the chosen amount of starch (Sobocat HC, Südstärke GmbH, Schrobenhausen, Germany), agar (Agar Powder, Dixia AG, St. Gallen, Switzerland) or gelatin (Gelatin from porcine skin, G2500, Sigma-Aldrich/Merck KGaA, Darmstadt, Germany) was dispersed in deionized water at a temperature of 40 °C for starch and gelatin or 100 °C for agar, while dissolved using another magnetic stirrer. Afterwards the two slurries were mixed together and stirred until homogenized. The gel-like slurry was poured into a 150 x 150 mm (internal dimensions) wide Fused Deposition Modeling (FDM) printed mold, which consists of a lower lid and a 11 mm high spacer screwed to it. After the slurry was spread uniformly using a spatula, the upper lid was placed on top and fixed in place by tightening it using screws. The closed mold was pre-cooled in a fridge at 4 °C for at least 8 hours and subsequently placed in a freezer (TUS 80-100 LOGG, FRYKA-Kältetechnik GmbH, Esslingen, Germany) at −80 °C for at least 24 hours. Afterwards the mold was taken out of the freezer, and the upper and lower lid was replaced with a lid featuring 225 5 mm diameter holes for enabling evaporation. The still frozen mold and specimen were placed on the metal racks in the glass chamber of a laboratory freeze-dryer (Alpha 3-4 LSCbasic, Martin Christ Gefriertrocknungsanlagen GmbH, Osterode, Germany) and freeze-dried for at least 72 hours at a pressure of 0.05 mbar. All cryogels exhibited a volumetric shrinkage of less than 5%. After drying the plates were removed from the molds and cut into the required shapes using a laser cutter (Nova24 60 W, Thunder Laser Tech Co., Ltd., Shatian, China). Furthermore, a FDM-printed grinding jig featuring sanding paper was used to manually grind the height of the samples to the required dimensions. An overview of the manufacturing process is given in Figure 3a.

Printed sensors

To enable proprioceptive and environmental sensing capabilities at a low environmental impact, the sensors were printed from a carbon black based conductive ink. To achieve rapid prototyping iteration cycles, low-cost manufacturing and full control over the printed geometry, ink-jet printing was selected. A commercial ink-jet printer (ET-1170, Seiko Epson Corporation, Tokyo, Japan) featuring a refillable ink-storage tank was chosen to enable testing of various conductive inks. The proposed sensing skin was printed using carbon-black nanoparticle ink (JR-700LV, NovaCentrix, Austin, USA) on low-roughness electronics paper substrate (PowerCoat XD 80, Arjowiggins Ltd., Aberdeen, UK). It was found that the structures printed at the highest volumetric deposition setting, did not achieve the anticipated conductivity. To mitigate this, several layers of deposited ink were printed on the substrate. Analyzing the conductivity depending on the number of passes showed that a minimum resistivity was achieved at three consecutive passes. Various curing methods (thermal-, UV- and air-curing) of the printed structures were investigated. The tests conducted showed that air-curing resulted in the lowest resistivity, nevertheless requiring the longest drying time. To speed up the drying process the printed structures were placed on a heating pad set to 40 °C. Doing so a resistance of 7.3 kΩ per square was achieved. The printing process is summarized in Figure 3b.

To achieve real-time information on the position of the elevons of the flying wing, printed bending sensors were embedded onto the wing. The sensors were placed on the deflecting section of the elevon spanning half of the wing-span. The final sensor was designed to feature 438 kΩ of total resistance, which corresponds to 60 squares with the given sheet resistance. For each elevon one of the sensors was utilized. For collecting environmental data such as the ambient temperature, another sensor was printed on the paper substrate at the fuselage section of the wing. For realizing the temperature sensor a 500 kΩ resistor (16 mm long and 9 mm wide) was chosen and coated using bee-wax. Both resistive sensors are connected via Zinc wires with a custom-developed sensor terminal, located on the fuselage section. An overview of the sensor layout and

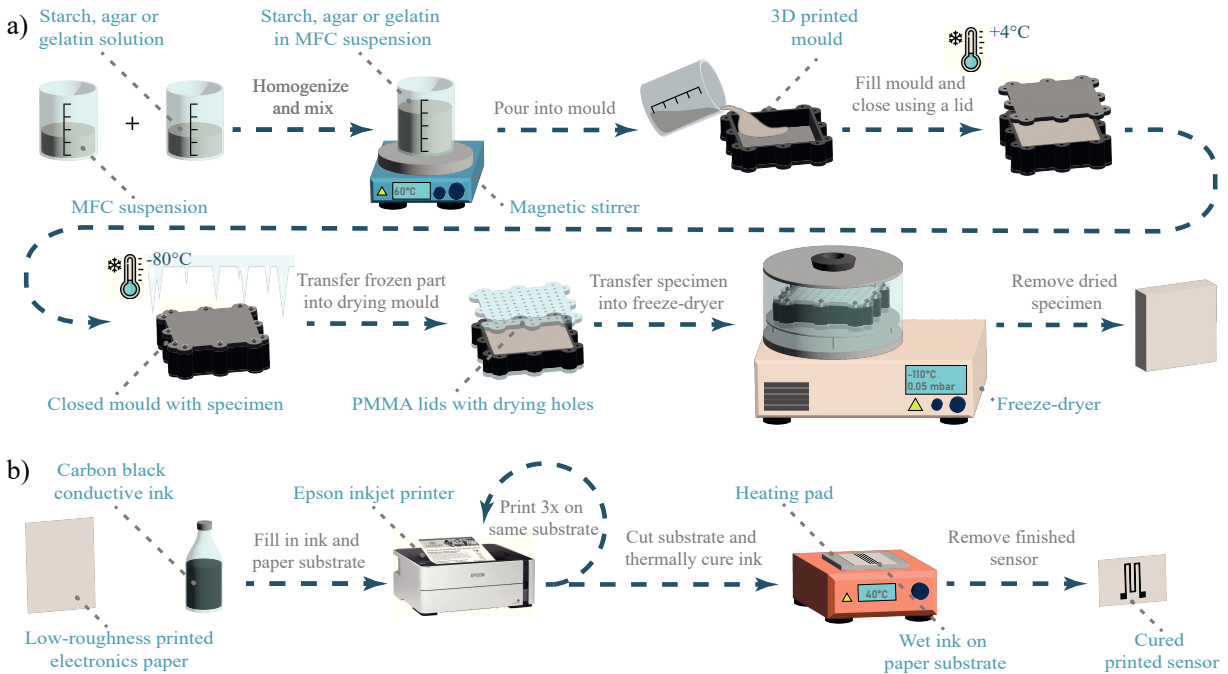


Figure 3: Manufacturing process flowchart. **a)** For the cryogel air-frame the MFC suspension and the starch, agar or gelatin solution are homogenized using a magnetic stirrer and the slurry is poured into a 3D-printed square mold. The mold is closed and placed in a refrigerator. After 8 hours the specimen is transferred into a -80 °C freezer overnight. Afterwards the lids are swapped with PMMA lids featuring drying holes and the assembly is placed in a freeze drier for at least 72 hours. The finished specimen is removed and cut into the desired size using a laser cutter. **b)** Sensing skin manufacturing process flowchart. The low-roughness electronics paper was placed in the paper tray of the printer. Afterwards the carbon conductive ink was printed three times at the same locations. The wet sensor was then cured using a heating pad.

the integrated flying wing demonstrator is given in Figure 4a. Details on the fabrication of the flying wing demonstrator are given in the supporting information 1.1.1.

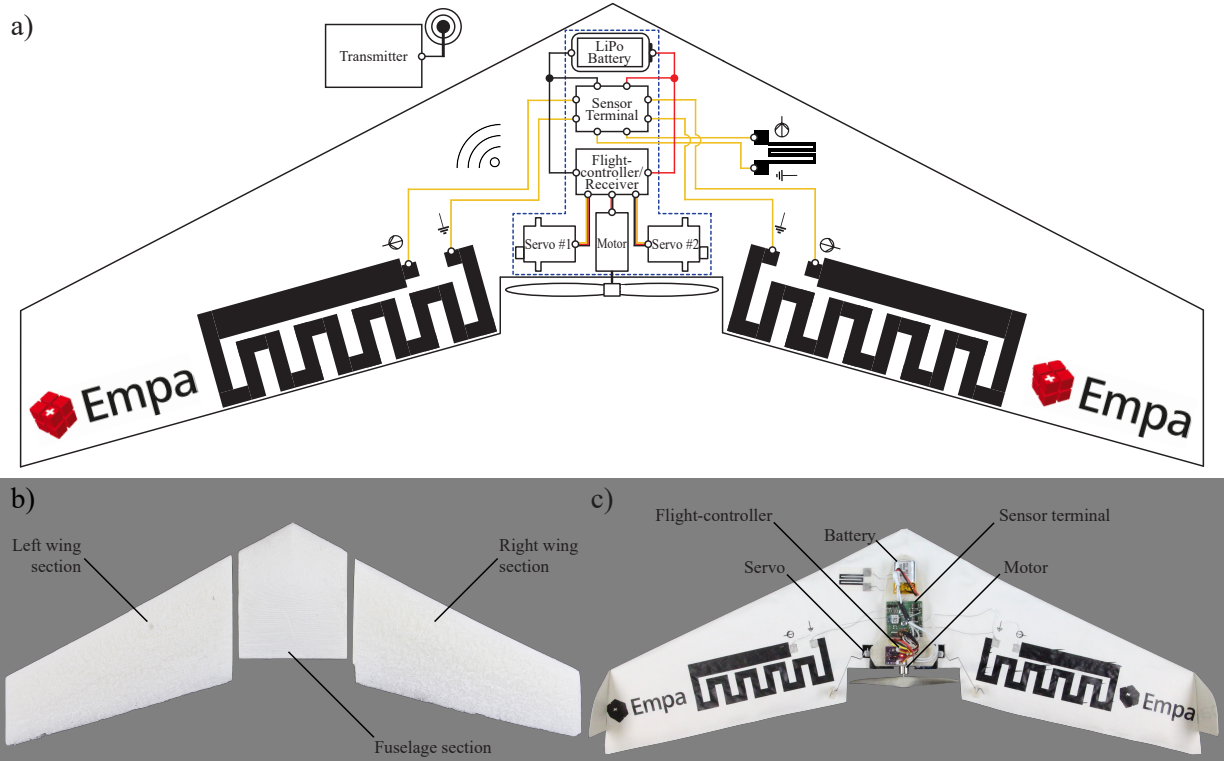


Figure 4: Overview of the drone. **a)** System-architecture overview of the transient drone indicating the proprioception and exteroceptive sensor layout integrated on the sensing skin. The deflection sensors are located on each wing close to the trailing edge, while the temperature sensor is located on the fuselage section. The battery, the sensor terminal, the flight controller/receiver, the motor as well as the servo motors are indicated. The components mounted to the electronics housing are indicated with a dashed blue line. **b)** Cryogel cores before bonding the wing sections to the fuselage section. **c)** Finished drone with the electronics mounted to the housing and the sensors connected with the sensor terminal. For better representation the hood is not closed in this photograph.

Results and discussion

In this section, the mechanical properties of the cryogels are summarized and the micro-structure based on scanning electron microscopy (SEM) images and μ -Computer Tomography (μ -CT) scans are characterized. Furthermore, the biodegradation of the investigated materials is quantified and the performance of the sensing skin is investigated. In the end, the drone testing results are presented.

Cryogel mechanical properties

The mechanical properties of the manufactured samples were evaluated through compression tests using a mechanical testing machine (Z100 AllroundLine, ZwickRoell GmbH & Co. KG, Ulm, Germany) in combination with a 1 kN load-cell and two 160 mm diameter circular compression plates made from steel. For calculating the compressive modulus E_c as well as the compressive strength σ_c the tests were performed on the basis of ASTM D1621 (ASTM International, 2016). A minimum of three 35 mm by 35 mm large square samples were cut from the 11 mm thick cryogel plates using a CO_2 laser cutter (Nova24 60 W, Thunder Laser Tech Co., Ltd., Shatian, China) operated at 75 % power and 30 mm sec^{-1} cutting speed. The samples were then ground to a nominal thickness of 10 mm using a custom 3D-printed grinding jig. The

samples were placed in the center of the compression plates and compressed at a rate of 1 mm min^{-1} . The apparent modulus as well as the strength based on 10% deformation were calculated using a Matlab (The MathWorks, Inc., Natick, Massachusetts, USA) script. To calculate the specific compressive stiffness as well as the specific compressive strength the individual sample masses were detected using a precision balance (Kern PCB 250-3, KERN & SOHN GmbH, Balingen-Frommern, Germany). Figure 5a summarizes the specific stiffness in $kPa g^{-1} cm^3$ of the composite-cryogels made from MFC with starch, agar or gelatin, while Figure 5b gives the specific strength in $kPa g^{-1} cm^3$ of the same cryogels. Figure 5c summarizes the specific stiffness in $kPa g^{-1} cm^3$ of the plain cryogels made from a 6wt% slurry or suspension of MFC, starch, agar and gelatin, while Figure 5d gives the values of the specific strength in $kPa g^{-1} cm^3$ for the same cryogels. For comparison the specific stiffness of the 6% MFC:G has a specific stiffness of $10.39 \cdot 10^4 kPa g^{-1} cm^3$ ($s = \pm 3.07 \cdot 10^4 kPa g^{-1} cm^3$) and a specific strength of $4'754 kPa g^{-1} cm^3$ ($s = \pm 848 kPa g^{-1} cm^3$).

To model the mechanical properties of the foams depending on the relative density, Gibson and Ashby's (Gibson and Ashby, 1997) cellular solids model was deployed. According to them the porosity of a foam P is given by Equation 1, where $\frac{\rho^*}{\rho_s}$ corresponds to the relative density, which is expressed as the density of the foam ρ^* divided by the density of the cell wall material ρ_s . The densities of the cell wall material were calculated using the rule of mixture. Doing so the two phases n and their respective weight fraction w_i were used to calculate ρ_s .

$$P = 1 - \frac{\rho^*}{\rho_s}, \quad \frac{1}{\rho_s} = \sum_{n=1}^n \frac{w_i}{\rho_i} \quad (1)$$

An overview of the densities of the measured foams, the computed cell wall material densities as well as the calculated average porosities of the foams are given in Table 2 in section 1.3.2 in the supporting materials. Note that the values for MFC:S at 1wt% total and MFC:G at 1wt% total are not given. The foams collapsed already during handling and therefore no reliable data was measured. The standard deviation for each value is given in brackets. According to Gibson and Ashby (Gibson and Ashby, 1997) the scaling laws of the Young's Modulus and strength for open cell foams are given by Equation 2, where E_s is the modulus of the solid cell wall material and E^* is the modulus of the foam, while σ_s and σ^* correspond to the yield strength of the solid cell wall material and the compressive strength of the foam.

$$\frac{E^*}{E_s} = \left(\frac{\rho^*}{\rho_s}\right)^2, \quad \frac{\sigma^*}{\sigma_s} = 0.3 \left(\frac{\rho^*}{\rho_s}\right)^{\frac{3}{2}} \quad (2)$$

For estimating E_s and σ_s the measured values of E^* and σ^* in relation to the relative density $\left(\frac{\rho^*}{\rho_s}\right)$ were plotted in Figure S1a and S1b respectively in section 1.2.1 in the supporting materials. Fitting polynomial regressions to the power of 2 for the Young's Modulus and to the power of $\frac{3}{2}$ for the strength, the acquired data can be used to calculate E_s and σ_s . The determined values for the stiffness and strength are provided in the supporting materials in Table S2 in section 1.3.2. For MFC:S a stiffness of $494.1 MPa$ and a strength of $23.61 MPa$, for MFC:A a stiffness of $150.4 MPa$ and strength of $12.05 MPa$, and for MFC:G a stiffness of $2'616.0 MPa$ and a strength of $93.07 MPa$ were found.

The sensors were printed on low-roughness electronics paper substrate and were used as a sensing skin. This skin was bonded to the stiff and strong cryogel cores of the two wing sections and the fuselage section, resulting in a sandwich-structured composite. To evaluate the strengthening effect of the skin bonding, three-point bending tests have been conducted using a mechanical testing machine (Z005 AllroundLine, ZwickRoell GmbH & Co. KG, Ulm, Germany) in combination with a $1kN$ load-cell and an adjustable three-point bending setup made from steel. For calculating the flexural stiffness E_B , as well as the flexural strength σ_{fM} the tests were performed on the basis of ASTM D790 (ASTM International, 2020). Nine 22 mm wide and 140 mm long samples were cut out of 6 wt% MFC:G plates using the CO_2 laser cutter operated at 75 % power and 30 mm sec cutting speed. Using a 3D-printed grinding jig the samples were ground to a

nominal core thickness of 9 mm, which is the same height as the cord-root of the drone’s wing. Afterwards the electronics paper was bonded on top and bottom of the foam core samples. The specimens were placed on the two supports ($R_1 = 5$ mm) of the three-point flexural rig at a support span length of 90 mm and the loading head ($R_2 = 5$ mm) was moved downwards at a rate of 6mm min^{-1} . To decrease the effect of introduced cover sheet buckling, 22 mm wide, 25 mm long and 3 mm thick rubber pads with a Shore 60 A (Mold Max 60, Smooth-On Inc., Macungie, USA) were placed between the sample and the three loading positions. The flexural modulus as well as the strength were calculated following the guidelines given by ASTM D790. The individual sample masses were detected using a precision balance (Kern PCB 250-3, Kern & Sohn GmbH, Balingen-Frommern, Germany). It was found that the samples without face sheets had a mean flexural stiffness of $E_B = 4'849$ MPa ($s = 706$ MPa) and a mean flexural strength of $\sigma_{fM} = 1.09$ MPa ($s = 0.25$ MPa), while the samples with face sheets achieved a mean flexural stiffness of $E_B = 13'585$ MPa ($s = 2'491$ MPa) and a mean flexural strength of $\sigma_{fM} = 2.15$ MPa ($s = 0.25$ MPa). Therefore, it was found that the flexural stiffness increased by a factor of 2.80 x, and the flexural strength increased by a factor of 1.97 x through the addition of the face sheets, while the weight increased by a factor of 1.31 x.

The characterizations have shown, that the mechanical properties of MFC:G composites are superior to the other binary compositions. It was found that especially the specific stiffness of MFC:G samples prepared from $4\text{wt}\%$ slurries and the specific strength of MFC:G samples prepared from $6\text{wt}\%$ slurries outperform most other biodegradable, isotropic and non-fossil foams discussed in the literature. Figure 5e summarizes this finding for the compressive modulus versus the material’s density, while Figure 5f indicates the high compressive strength versus the material’s density. Furthermore, the prepared starch and agar composites feature worse mechanical properties. Figure 5e indicates the performance indices for minimum weight design of the stiff beams and of the stiff plates, through the $4\text{wt}\%$ MFC:G composite. Considering the slender wing as a beam-like structure and the square fuselage section as a plate, the indices can guide the material selection. For manufacturing a stiff and lightweight structure, the wing section, as well as the fuselage, need to be manufactured from $4\text{wt}\%$ MFC:G cryogels. Figure 5f gives the performance indices for the minimum weight design of strong plates and strong beams. For designing a strong and lightweight fuselage the use of $6\text{wt}\%$ MFC:G would be favorable, while for a strong wing $8\text{wt}\%$ MFC:G would be the best choice. According to this the wings and the fuselage were manufactured from $4\text{wt}\%$ MFC:G.

Microstructure

To estimate the homogeneity of the developed cryogels, the micro-structure was investigated using SEM images and μ -CT scans. The SEM (Quanta 650 FEG ESEM, FEI, Hillsboro, Oregon, USA) images were taken at an accelerating voltage of 5keV . For retrieving insights into the cross-sectional morphology the cryogels were broken into two parts. Afterwards, the samples were sputtered with 7nm platinum (Bal-Tec MED 020 Modular High Vacuum Coating Systems, Bal-Tec AG, Liechtenstein). The resulting morphologies of the cryogels at a total weight content of $6\text{wt}\%$ (MFC:S, MFC:A, MFC:G) are shown in Figure 6a, e and i. To understand the volumetric morphology of the cryogels, their cell characteristics, and their pore size distributions, μ -CT (Easy Tom XL Ultra 230 – 160 micro/nano CT scanner, RX Solutions, Chavano, France) scans were taken. The μ -CT scanner operated at 45kV and a current of $180\mu\text{A}$ outputting a nominal resolution of $6\mu\text{m}$ (voxel size). The samples were scanned full 360° with a continuous rotation acquiring 1568 projection with a frame average of 4. Reconstruction of μ -CT slices was performed with dedicated software maintaining the same nominal resolution. A cubic volume of interest (VOI) of 5mm per side was considered in each sample for the morphological analysis. The $2D$ slices were segmented and the detected pores were separated computing the watershed lines using a chamfer matching algorithm. The distribution of pore size was calculated as equivalent diameter (Eq.D in μm). The separated $2D$ pores in each μ -tomographic section with a size of less than $17\mu\text{m}$ (object of 2×2 pixels) were excluded to reduce noise. The $3D$ representation, the pore-size distribution histogram as well as $2D$ cross-section views are given in Figure 6 b-d, f-h and j-l.

Videos indicating the porosity of each slice of the samples are provided in the supporting material movie S1.

Hosted file

Supporting Movie S1-1.mp4 available at <https://authorea.com/users/579772/articles/621096-high-performance-biopolymer-cryogels-for-transient-sensing-ecology-drones>

Starch is a polymeric carbohydrate consisting of two high molecular weight, polydisperse [1-4]- α -D-glucose polysaccharides: the highly branched amylose and the linear amylopectin (Koev et al., 2020). Benefiting from its ability to associate into a range of semi-crystalline forms, the starch polymers interweaved with MFC and formed aggregated structures during the process, leading to a porous structure. Agar is a mixture of small molecules, including β -D-galactose and 3, 6-lactone-L-galactose. During the freezing process, agar and MFC were consolidated and formed a structure with integrated large lamellas, as shown in Figure 6b. By contrast, the interweaved and cross-linked structures of MFC:S and MFC:G complexes make their cryogels show porous structures. Gelatin is a degradation of collagen, made of glycine, proline, and 4-hydroxy proline residues (Deshmukh et al., 2017). At temperatures above 40 °C, it has a random coil structure in solution, (He et al., 2018) and the formation of soluble MFC:G complexes via electrostatic attraction occurred. Once cooling below the coil-to-helix transition temperature of gelatin at around 4 °C, the polymer strongly intertwined each other to form ordered triple-helical segments by hydrogen bonding (Rousseva et al., 2012). At the same time, the gelatin bridged MFC into a complex and a colocalized biopolymer network (Wang et al., 2018). The great improvement of the mechanical strength of the MFC:G porous structure might indicate triple-helical segments forming during the freeze-drying (Cai et al., 2021). Furthermore, its superior structural performance is in accordance with other reports illustrating that porcine gelatin films achieve at least two times higher strength than films fabricated from potato starch (A. et al., 2013; Punia et al., 2021).

Biodegradation

For evaluating the degradation rate of the developed material system and the sensing skin, biodegradation tests of the investigated cryogel composites under accelerated conditions were performed. Conducting laboratory-scale tests to evaluate the disintegration rate under simulated aerobic composting conditions, the norm ISO 20200 was followed. The tests were performed for 70 days at constant 58 °C. The soil simulator was composed of sawdust, rabbit feed, cornstarch, sugar, corn oil, urea and compost. The samples were put inside a protective mesh made from polypropylene and buried entirely in the soil. The mass of the sample was then weighed with and without the protective mesh in week 0 to week 10, excluding week 9. The weight loss, as well as representative pictures of each sample at week 0, 1, 2, 3 and 10, are summarized in Figure 7.

It was found that the MFC:S and MFC:G samples degrade at a faster rate than the MFC:A samples. In accordance with the mechanical properties found, especially MFC:G combines fast degradation and high mechanical properties and therefore, is the most suitable candidate for manufacturing a lightweight, transient drone.

Sensing characteristics

To quantify the capabilities of the proposed low-cost sensors, the bending sensor as well as the temperature sensors were tested independently before integration into the eco-drone. For the characterization of the proprioception a mock-up wing section was manufactured from 6wt% MFC:G cryogel. The electronics paper featuring a bending sensor was bonded to the wing section and the wing was clamped with a 3D printed mount as seen in Figure 8a. After the installation of the servo motor and the rudder horn, the elevon was displaced, while the resistance of the sensor was continuously measured using a desktop multimeter (DMM6500 Desktop multimeter, Tektronix Inc., Beaverton, USA). First, the elevon was periodically displaced from -30° to 30° at a frequency of 1Hz. Afterwards a step-wise deflection was induced ranging from -30° to 30° at a 10° step-size. Each deflection was held for 60 seconds. Figure 8a shows the used testing setup and Figure 8b and 8c indicate the relative resistance change during the cyclic testing. Figure 8d indicates the relation between the deflection of the elevon and the corresponding relative resistance change. To characterize the exteroception capabilities of the proposed design, the temperature sensor was either not further treated or dip coated with

carnauba- or bee-wax. Afterwards the three sensors were connected to a data acquisition system (34970A, Agilent Technologies Inc., Santa Clara, USA) measuring the resistance change in a two-probe setup. The sensor was placed in a climatic chamber (Vötsch VC4100, Weiss Technik GmbH, Balingen, Germany) to create the desired temperature profile. The temperatures tested range from 15 °C to 35 °C at a constant relative humidity of 50% and each temperature was held for 2 hours. For each temperature step the average was computed and a scatter plot relating the temperature and the relative resistance change during the third cycle is shown in Figure 8e. To further understand the effect of humidity on the sensor and determine the best coating for the wing-integrated temperature sensor, tests have been conducted and the results are given in Figures S2a and S2b given in section 1.2.2 in the supporting materials. Figure S2 a summarizes the third cycle relative resistance change depending on the relative humidity in the range of 10% to 90% at constant 20 °, while Figure S2b summarizes the relative resistance change taken in the range of 15 °C to 35 °C at a constant absolute humidity of 5.7 g/cm³. Additionally, dynamic vapor sorption (DVS) tests were conducted using a bench-top DVS analyzer (Endeavour, Surface Measurement Systems Ltd., London, UK). The relative humidity was changed from 0% to 90% at a constant temperature of 20°. One un-treated paper sample, one carnauba-wax and bee-wax coated sample as well as one carnauba-wax coated sample with a printed resistor and one bee-wax coated sample with a printed resistor were analyzed. The results, which are summarized in the supporting materials section 1.2.3 in Figure S3, indicate that the coatings limit the mass uptake, with bee-wax performing the best. The data shows that the samples including a resistor feature a higher mass uptake than the blank samples.

The integrated bending sensors showed that changes in the elevon’s deflection at a resolution of at least 10 ° were detectable while indicating only minor hysteresis. In addition, the cyclic tests showed that the system had minor drift and performed well over the time tested. The integrated temperature sensor’s performance is highly dependent on the coating used. While carbon features a negative temperature coefficient, a linear negative trend is observed when plotting the relative resistance change. The flat curve indicates rather low sensitivity to temperature changes, while a clear linear relationship is exhibited and no hysteresis is observed. The sensors coated in bee-wax and carnauba-wax showed up to 19.12 x and 11.45 x higher sensitivity respectively. Due to the penetration of the ink and paper with wax, which generally features a high coefficient of thermal expansion (CTE), the carbon conductive ink itself expands when heated. This induces larger distances between the conductive particles in the ink and ultimately, results in an increase in resistance. Therefore, the sensitivity difference between the used bee-wax and carnauba-wax coated sensors is due to the 2.2 x higher CTE of carnauba wax (Craig et al., 1965). While the carnauba wax-coated sensor features a linear relationship between relative resistance change and temperature as well as no visible hysteresis, the bee-wax coated sensor suffers from some non-linearity as well as hysteresis, resulting in a relative resistance difference of up to 39.7% at 25 °C. This behavior is due to the lower melting point of beeswax. Nevertheless, the coated sensors are capable of measuring temperature down to a resolution of at least 5 °C. The information presented in supporting Figure S2 in section 1.2.2 in the supporting materials indicates, that the carnauba-wax coating fails to mitigate resistance changes induced by changing relative humidity. In contrast, the measured resistance of the bee-wax coated sensor does not change up to a relative humidity of 80%. Therefore, it can be said that the bee-wax coated temperature sensor decouples the humidity-induced effect better and has a superior performance.

Flying wing testing

A 410 mm wingspan flying wing with an MH44 airfoil was manufactured using 4wt% MFC:G. All the other components (vertical stabilizers, rudder horns, 3 inch diameter propeller, and electronics) were printed using a biodegradable Polyhydroxybutyrate 3D printing filament (AllPHA Natural, Colorfabb B.V., Belfeld, Netherlands). The electronics housing is used as a crash box containing all non-degradable components, such as a combined flight controller (FC) and electronic speed controller (ESC) (MA-RX42-D+, OverskyRC Co. Ltd., Wuhan, China), two 1.7 g servos for elevon actuation, a 100 mAh battery, a 16’000 Kv brushed motor as well as the custom sensor terminal printed circuit board (PCB), featuring a Bluetooth transmission module. The printed sensors were connected to the sensor terminal PCB using Zinc wires (Zinc wire, Thermo

Fisher Scientific Inc., Waltham, USA). While the deflection sensor reading was acquired using a Wheatstone bridge setup, the temperature sensor was analyzed utilizing a voltage divider. During testing, the control surfaces were remotely deflected, and the sensor terminal transmitted the voltage readings using Bluetooth to a ground station at a sampling frequency of 200 Hz. The received voltage was converted to the respective resistance reading and plots are given in Figure 9a and b for the right and left wing. Prior to plotting a moving average filter with a window size of 100 readings was deployed. When a heat gun was pointed at the bee-wax coated temperature sensor an increase in resistance was visible. The measured signal after filtering is shown in Figure 9c. A total resistance change of 54 kOhm was detected, which corresponds to a relative resistance change of 7.27%. Using the data presented in Figure 9e as a calibration curve, a local temperature increase of 9.66 °C was measured.

Range tests have shown that the data can be transmitted up to a range of 85 meters, making the systems capable of medium-range environmental sensing flights. Further details on the design and manufacturing of the drone as well as the sensor terminal PCB are given in the supporting materials section 1.1.1, 1.2.4 and 1.1.2 respectively. Videos of the lab-bench tests and outdoor flight tests of the developed cryogel drone can be found below.

Hosted file

Supporting Movie S2-1.mp4 available at <https://authorea.com/users/579772/articles/621096-high-performance-biopolymer-cryogels-for-transient-sensing-ecology-drones>

Hosted file

Supporting Movie S3-1.mp4 available at <https://authorea.com/users/579772/articles/621096-high-performance-biopolymer-cryogels-for-transient-sensing-ecology-drones>

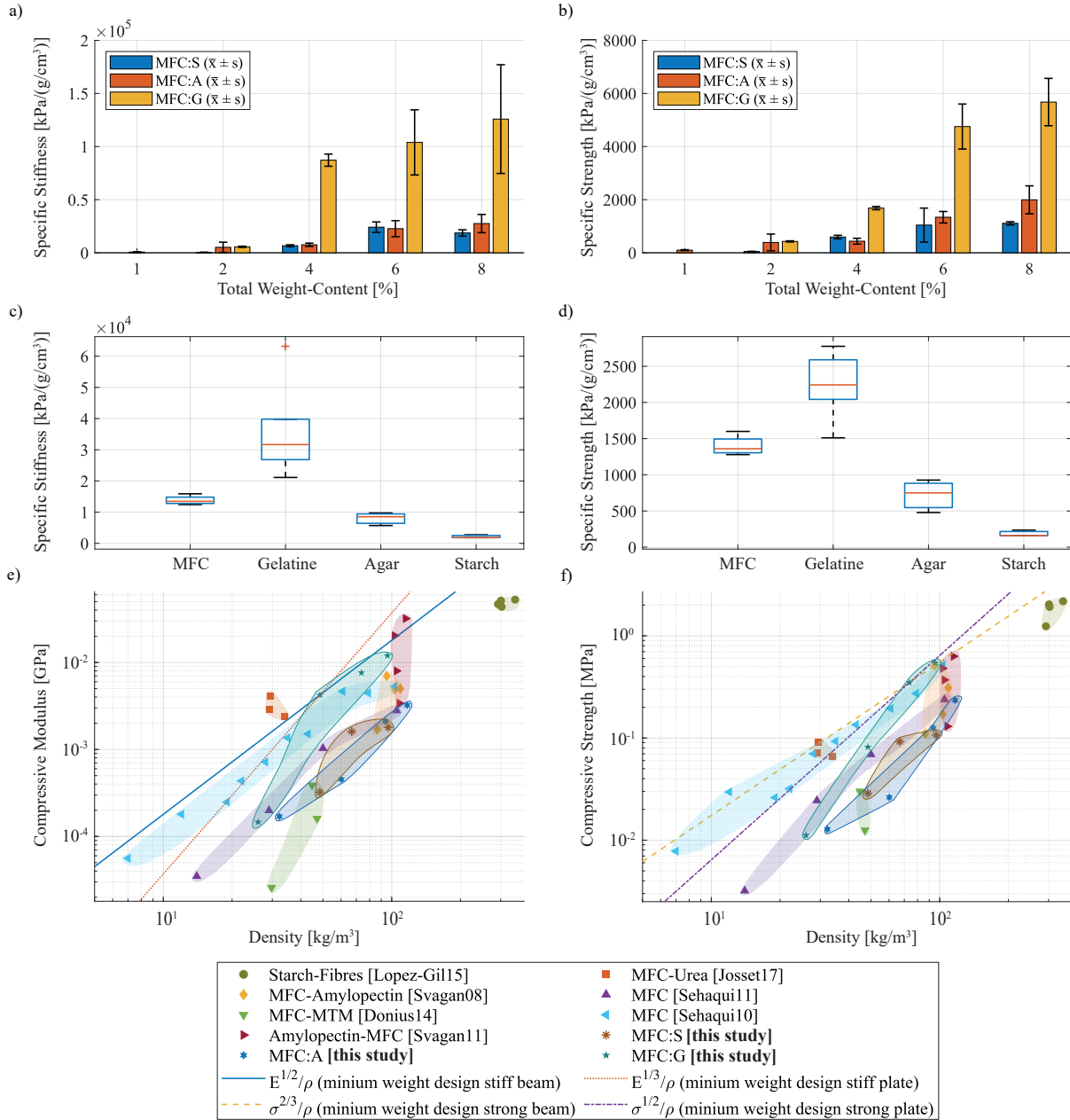


Figure 5: Overview of the mechanical properties of the investigated biopolymer cryogels. The mean values and the standard deviations are given as well as two Ashby plots comparing the properties of other isotropic, biodegradable and non-fossil foams (Lopez-Gil et al., 2015; Josset et al., 2017; Svagan et al., 2008; Sehaqui et al., 2011; Donius et al., 2014; Sehaqui et al., 2010; Svagan et al., 2011) are given. **a)** Specific stiffness in $\text{kPa}/\text{g}^{-1}\text{cm}^3$ of the MFC:S, MFC:A and MFC:G cryogels at 1%, 2%, 4%, 6% and 8% weight-content. **b)** Specific strength in $\text{kPa}/\text{g}^{-1}\text{cm}^3$ of the MFC:S, MFC:A, MFC:G cryogels at 1%, 2%, 4%, 6% and 8% weight-content. **c)** Specific stiffness in $\text{kPa}/\text{g}^{-1}\text{cm}^3$ of the plain cryogels at a total weight content of 6%. **d)** Specific strength in $\text{kPa}/\text{g}^{-1}\text{cm}^3$ of the plain cryogels at a total weight content of 6%. **e)** Ashby plot giving the compressive modulus versus the density of the starch, agar and gelatin composites and comparing it with other materials. The guidelines for minimum weight design of stiff beams and of stiff plates are given through the best performing gelatin composite of this study (4wt%). **f)** Ashby plot giving the compressive strength versus the density of the starch, agar and gelatin composites and comparing it with other materials. The guidelines for minimum weight design of strong beams and of strong plates are given through the best performing gelatin composite of this study (6wt%). 13

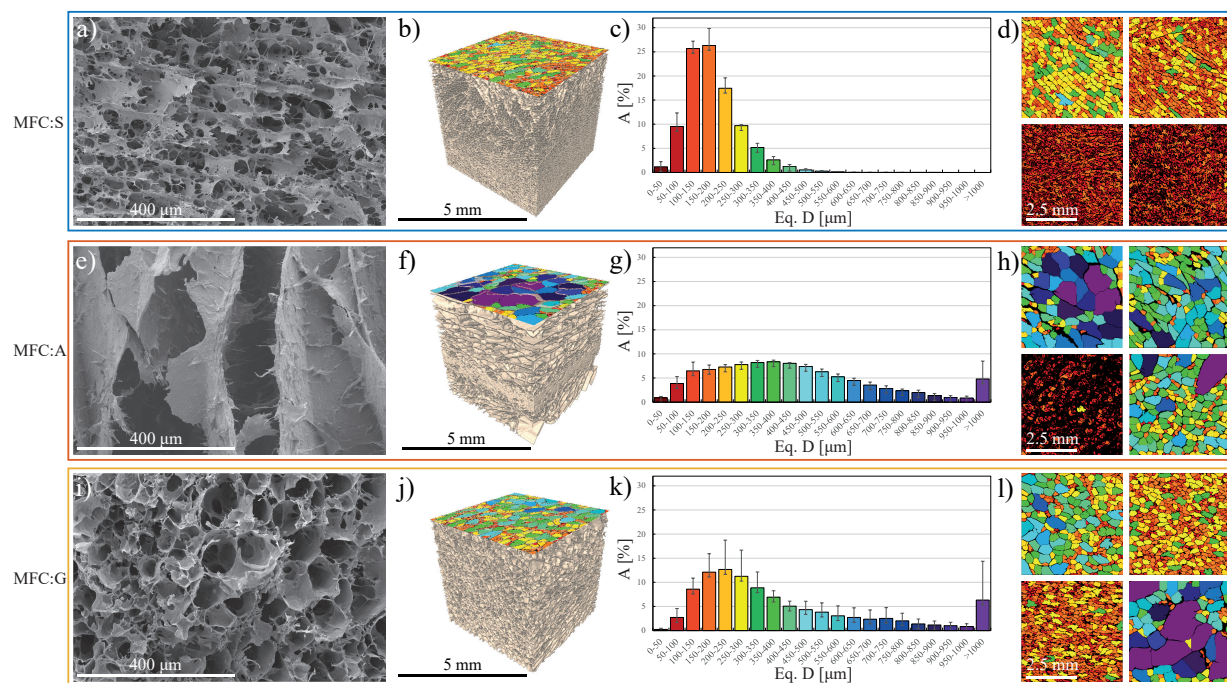


Figure 6: Overview of the cross-sectional morphology of the MFC:S, MFC:A and MFC:G crygel composites made from suspensions/solutions with a total weight content of 6%. The SEM images were generated at an accelerating voltage of 5kV. The mu-CT scans were acquired with a X-ray source voltage of 45 kV. The colors correspond to the color-coded bars of the equivalent diameter ranges in μm . For visualization, 2D axial views of slices taken in the first, second, third and fourth quarters of the VOI of the materials are given in the right column. **a)** Cross-section of the total 6wt% MFC:S crygel at a magnification of $10^4\times$. **b)** 3D model of a 125mm^3 volume made from 6wt% MFC:S. **c)** Histogram of the pore size distribution as area occupied in % grouped in different intervals of equivalent diameters of 6wt% MFC:S. **d)** 2D $\mu\text{-CT}$ slices of 6wt% MFC:S cryogels. **e)** Cross-section of the total 6wt% MFC:A crygel at a magnification of $10^4\times$. **f)** 3D model of a 125mm^3 volume made from 6wt% MFC:A. **g)** Histogram of the pore size distribution as area occupied in % grouped in different intervals of equivalent diameters of 6wt% MFC:A. **h)** 2D $\mu\text{-CT}$ slices of 6wt% MFC:A cryogels. **i)** Cross-section of the total 6wt% MFC:G crygel at a magnification of $10^4\times$. **j)** 3D model of a 125mm^3 volume made from 6wt% MFC:G. **k)** Histogram of the pore size distribution as area occupied in % grouped in different intervals of equivalent diameters of 6wt% MFC:G. **l)** 2D $\mu\text{-CT}$ slices of 6wt% MFC:G cryogels.

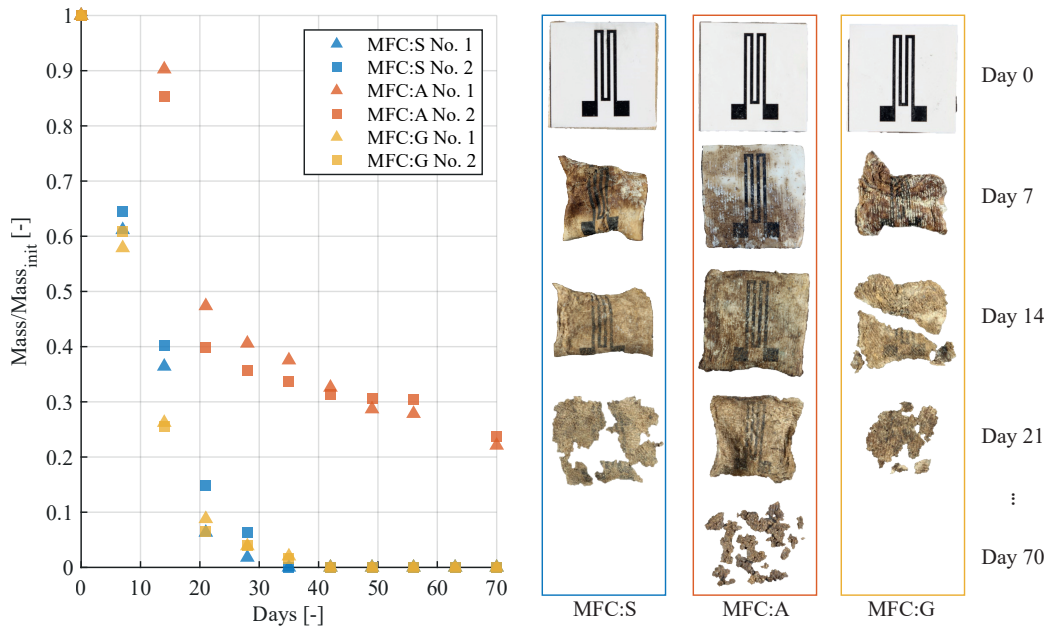


Figure 7: The weight loss of the investigated composites with bonded sensing skin. For week 0, 1, 2, 3 and 10 an image of a sample is given. The MFC:S and MFC:G samples have reached full disintegration after 5 and 6 weeks respectively.

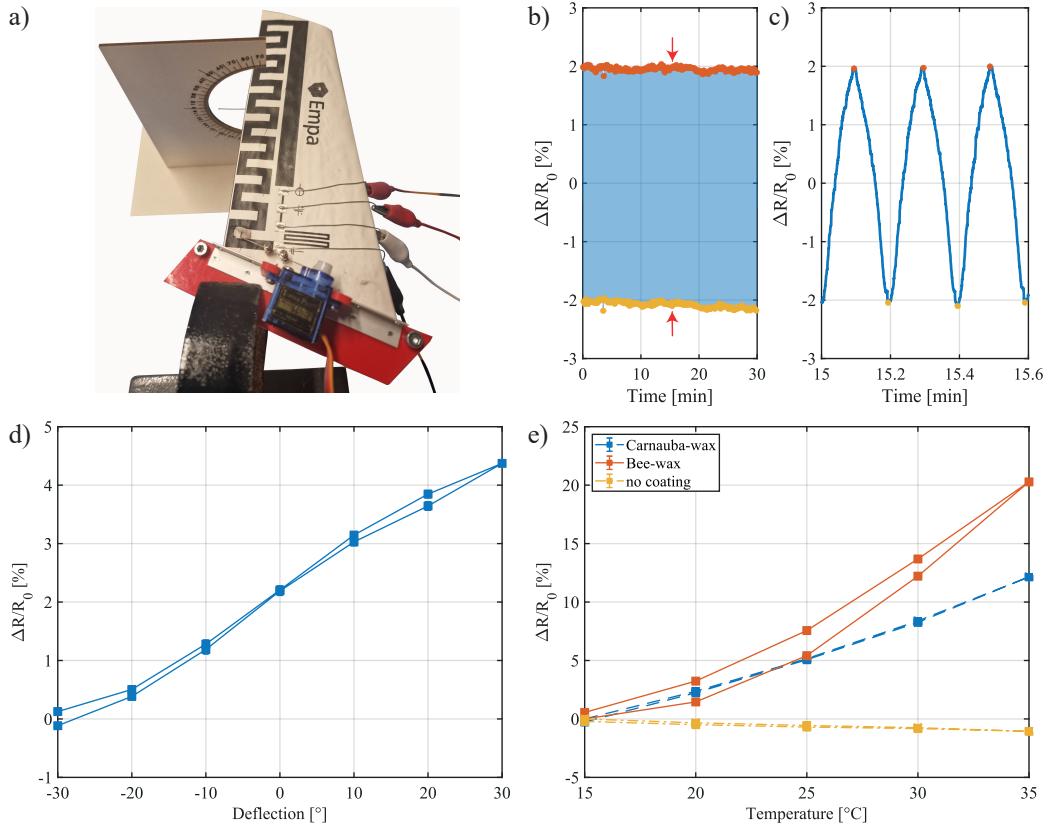


Figure 8: Sensing capabilities of the proposed drone. **a)** Flying wing section with integrated sensors clamped for proprioception characterization. **b)** Normalized, relative resistance change for 150 cycles changing the deflection from -30° to 30° at a frequency of 0.08 Hz. Each cycle's maximum and minimum are highlighted in red and yellow respectively. **c)** Zoomed-in view of the normalized, relative resistance change at 15 minutes. **d)** Normalized, relative resistance change of the deflection sensor. The elevon angle was adjusted from -30° to 30° in 5° degree steps. Each angle was held for 60 seconds and the measured average was plotted. **e)** Normalized, relative resistance change of the printed temperature sensor versus ambient temperature ranging from 15°C to 35°C in 5°C steps. The temperature sensor coated in carnauba-wax, bee-wax and without coating has been investigated at a constant relative humidity of 50%, while each temperature plateau has been held constant for 2 hours.

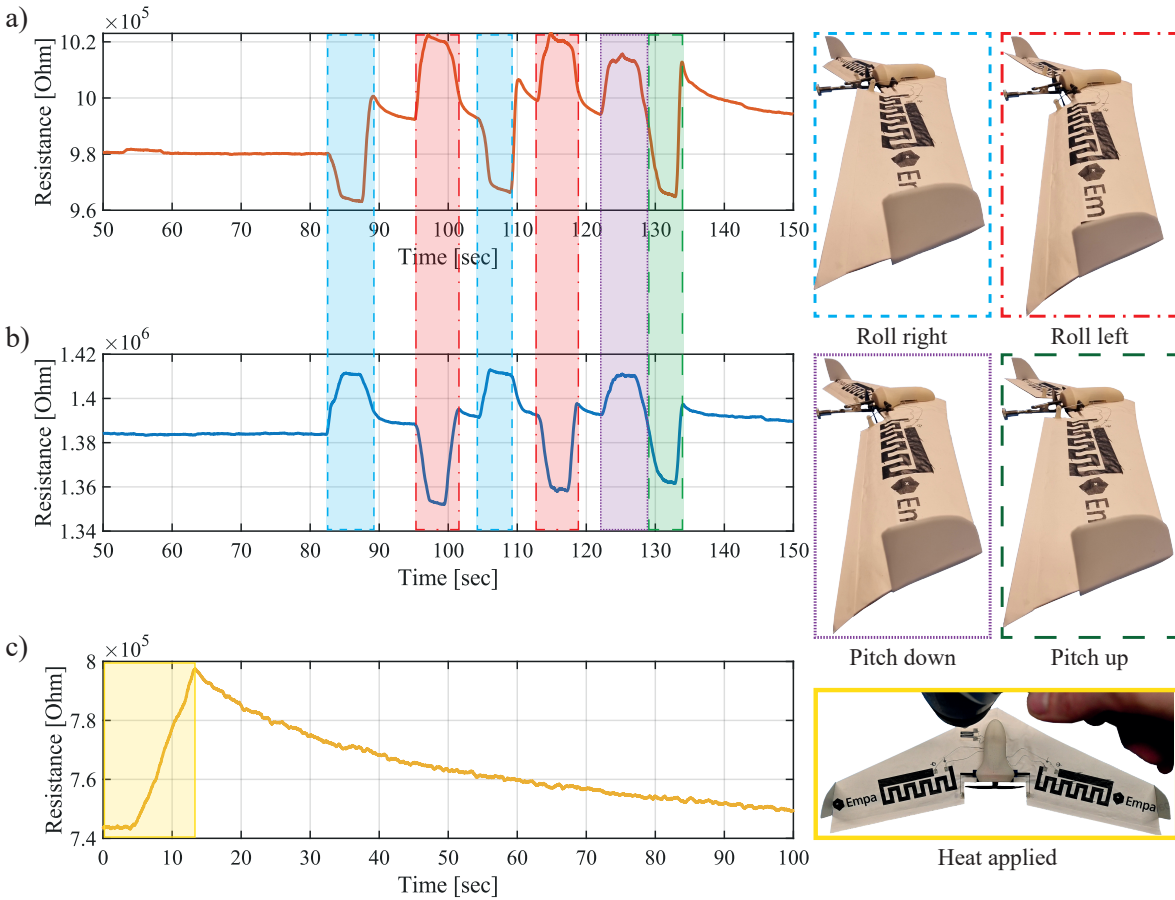


Figure 9: Testing of the integrated drone prototype. **a)** Post-processed signal of the right wing's sensing skin, during rolling to the right and left as well as pitching down and up. **b)** Post-processed signal of the left wing's sensing skin, during rolling to the right and left as well as pitching down and up. **c)** Transmitted resistance of the temperature sensors, when heated with a heat gun.

Conclusion

In this work, we have described manufacturing methods for generating lightweight and biodegradable structures through lyophilization and we presented a material design and manufacturing process for transient aerial drones. It was found that micro-fibrillated cellulose and gelatin composites feature superior mechanical properties over the here tested bio-polymer composite mixtures. Using this proposed manufacturing technique, more complex geometries were molded. The material's capabilities were showcased through the manufacturing of a lightweight flying wing drone, designed for environmental monitoring. Through the integration of low-cost ink-jet printed, eco-friendly sensors, self-sensing and temperature-sensing skin was manufactured and integrated into the proposed transient drone design. The integrated sensors showed good performance in measuring the bending angle of the elevons, while the temperature sensor was capable of estimating the ambient temperature. Furthermore, it was shown that the chosen materials feature quick biodegradation and can be used for one-way missions in sensitive environments. The test flight showed that the proposed design achieves high agility while enabling efficient monitoring flights. Overall tools were presented that can be used to manufacture the next generation of lightweight transient drones with integrated proprioception and environmental sensing capability.

To further develop the transient drone concept, further efforts should focus on the miniaturization of the required conventional electronics and the development of fully biodegradable components. The next steps could be the integration of biodegradable elevon actuators or the use of Zinc-air-based batteries (Poulin et al., 2022). Additionally, other materials than carbon particles could be explored to realize resistive sensors (Aeby et al., 2022). For example, zinc- or magnesium-based ink could reduce the environmental impact of the sensors, while achieving higher conductivity. When considering higher levels of autonomy of the drone, the added non-degradable electronics and mass need to be considered and evaluated beforehand. Nevertheless, the developed platform can be used to carry various transient sensing devices, such as humidity or UV-intensity sensors.

Supporting Information

Supporting Information is available from the Wiley Online Library or from the author.

Acknowledgements

We thank Anja Huch for preparing the SEM images and Roman Elsener for providing his expertise in using the mechanical testing machine. Furthermore, we would like to thank Katrin Hoffmann for the preparation of the MFC, Yusuf Furkan Kaya for contributing the conceptual illustration, David Häusermann for the engineering support, Max Widmer for piloting the drone as well as Roger Vonbank, Bruno Binder and Ivan Lunati for experimental support and fruitful discussions. We also thank Luis Nicklaus Caceres and Claudio Sommer for soldering the sensor terminal PCBs.

This work was supported in part by EPSRC Awards EP/R009953/1, EP/L016230/1, and EP/R026173/1, in part by NERC Award NE/R012229/1, in part by the EU H2020 AeroTwin project under Grant ID 810321, in part by the Royal Society Wolfson fellowship and in part by the Empa-Imperial research partnership.

Conflict of interest

The authors declare no conflict of interest.

Data Availability Statement

The data that support the findings of this study are available from the corresponding author upon reasonable request.

References

- Nur Hanani A., E. Beatty, Yrjö Roos, Michael Morris, and Joe Kerry. Development and Characterization of Biodegradable Composite Films Based on Gelatin Derived from Beef, Pork and Fish Sources. *Foods*, 2: 1–17, 01 2013. doi: 10.3390/foods2010001.
- Xavier Aeby, James Bourelly, Alexandre Poulin, Gilberto Siqueira, Gustav Nyström, and Danick Briand. Printed Humidity Sensors from Renewable and Biodegradable Materials. *Advanced Materials Technologies*, page 2201302, 11 2022. ISSN 2365-709X. doi: 10.1002/admt.202201302.
- Sandeep Ahankari, Pradyumn Paliwal, Aditya Subhedar, and Hanieh Kargarzadeh. Recent Developments in Nanocellulose-Based Aerogels in Thermal Applications: A Review. *ACS Nano*, 15(3):3849–3874, 2021. doi: 10.1021/acsnano.0c09678. URL <https://doi.org/10.1021/acsnano.0c09678>. PMID: 33710860.
- Carlo Antonini, Tingting Wu, Tanja Zimmermann, Abderrahmane Kherbeche, Marie Jean Thoraval, Gustav Nyström, and Thomas Geiger. Ultra-porous nanocellulose foams: A facile and scalable fabrication approach, 2019. ISSN 20794991.
- ASTM International. Standard test method for compressive properties of rigid cellular plastics. Technical report, ASTM International, 2016.
- ASTM International. Standard Practice for Determining Sandwich Beam Flexural and Shear Stiffness. Technical report, 2020.
- William L. Bauerle, Joseph D. Bowden, G. Geoff Wang, and Mohamed A. Shahba. Exploring the importance of within-canopy spatial temperature variation on transpiration predictions, 2009. ISSN 00220957.
- Nela Buchtová, Christophe Pradille, Jean-Luc Bouvard, and Tatiana Budtova. Mechanical properties of cellulose aerogels and cryogels. *Soft Matter*, 15:7901–7908, 2019. doi: 10.1039/C9SM01028A. URL <http://dx.doi.org/10.1039/C9SM01028A>.
- Suzhi Cai, Zhifang Sun, He Wang, Xiaokang Yao, Huili Ma, Wenyong Jia, Shuxu Wang, Zhihao Li, Huifang Shi, Zhongfu An, Yasuhiro Ishida, Takuzo Aida, and Wei Huang. Ultralong Organic Phosphorescent Foams with High Mechanical Strength. *Journal of the American Chemical Society*, 143(39):16256–16263, 2021. ISSN 15205126. doi: 10.1021/jacs.1c07674.
- Ricardo Cavicchioli, William J. Ripple, Kenneth N. Timmis, Farooq Azam, Lars R. Bakken, Matthew Baylis, Michael J. Behrenfeld, Antje Boetius, Philip W. Boyd, Aimée T. Classen, Thomas W. Crowther, Roberto Danovaro, Christine M. Foreman, Jef Huisman, David A. Hutchins, Janet K. Jansson, David M. Karl, Britt Koskella, David B. Mark Welch, Jennifer B.H. Martiny, Mary Ann Moran, Victoria J. Orphan, David S. Reay, Justin V. Remais, Virginia I. Rich, Brajesh K. Singh, Lisa Y. Stein, Frank J. Stewart, Matthew B. Sullivan, Madeleine J.H. van Oppen, Scott C. Weaver, Eric A. Webb, and Nicole S. Webster. Scientists’ warning to humanity: microorganisms and climate change, 2019. ISSN 17401534.
- R.G. Craig, J.D. Eick, and F.A. Peyton. Properties of Natural Waxes Used in Dentistry. *Journal of Dental Research*, 44(6):1308–1316, nov 1965. doi: 10.1177/00220345650440063301. URL <https://doi.org/10.1177%2F00220345650440063301>.
- Diego Debruyne, Raphael Zufferey, Sophie F. Armanini, Crystal Winston, Andre Farinha, Yufei Jin, and Mirko Kovac. MEDUSA: A Multi-Environment Dual-Robot for Underwater Sample Acquisition. *IEEE Robotics and Automation Letters*, 5(3):4564–4571, 2020. ISSN 23773766. doi: 10.1109/LRA.2020.3001534.

- K. Deshmukh, M. Basheer Ahamed, R.R. Deshmukh, S.K. Khadheer Pasha, P.R. Bhagat, and K. Chidambaram. 3 - Biopolymer Composites With High Dielectric Performance: Interface Engineering. In K.K. Sadasivuni, D. Ponnamma, J. Kim, J.-J. Cabibihan, and M.A. AlMaadeed, editors, *Biopolymer Composites in Electronics*, pages 27–128. Elsevier, 2017. ISBN 978-0-12-809261-3. doi: <https://doi.org/10.1016/B978-0-12-809261-3.00003-6>. URL <https://www.sciencedirect.com/science/article/pii/B9780128092613000036>.
- Amalie E. Donius, Andong Liu, Lars A. Berglund, and Ulrike G.K. Wegst. Superior mechanical performance of highly porous, anisotropic nanocellulose-montmorillonite aerogels prepared by freeze casting. *Journal of the Mechanical Behavior of Biomedical Materials*, 37:88–99, 2014. ISSN 18780180. doi: 10.1016/j.jmbbm.2014.05.012.
- FAO and UNEP. The State of the World’s Forests 2020. Forests, biodiversity and people., 2020. URL <http://www.fao.org/documents/card/en/c/ca8642en>.
- André Farinha, Raphael Zufferey, Peter Zheng, Sophie F. Armanini, and Mirko Kovac. Unmanned Aerial Sensor Placement for Cluttered Environments. *IEEE Robotics and Automation Letters*, 5(4):6623–6630, 2020. ISSN 23773766. doi: 10.1109/LRA.2020.3015459.
- Carlos M.S. Figueiredo, Eduardo F. Nakamura, Afonso D. Ribas, Thales R.B. De Souza, and Raimundo S. Barreto. Assessing the communication performance of wireless sensor networks in rainforests. In *2009 2nd IFIP Wireless Days, WD 2009*, 2009. ISBN 9781424456604. doi: 10.1109/WD.2009.5449672.
- Jonas Garemark, Xuan Yang, Xia Sheng, Ocean Cheung, Licheng Sun, Lars A. Berglund, and Yuanyuan Li. Top-Down Approach Making Anisotropic Cellulose Aerogels as Universal Substrates for Multifunctionalization. *ACS Nano*, 14(6):7111–7120, 2020. doi: 10.1021/acsnano.0c01888. URL <https://doi.org/10.1021/acsnano.0c01888>. PMID: 32413254.
- Lorna J. Gibson and Michael F. Ashby. *Cellular Solids, Structure and Properties*. Cambridge University Press, Cambridge, 1997.
- Qingyan He, Huang Yan, and Shaoyun Wang. Hofmeister Effect-Assisted One Step Fabrication of Ductile and Strong Gelatin Hydrogels. *Advanced Functional Materials*, 28:1705069 – 1705069, 2018.
- Sébastien Josset, Paola Orsolini, Gilberto Siqueira, Alvaro Tejado, Philippe Tingaut, and Tanja Zimmermann. Energy consumption of the nanofibrillation of bleached pulp, wheat straw and recycled newspaper through a grinding process. *Nordic Pulp and Paper Research Journal*, 29(1):167 – 175, 2014. doi: 10.5281/zenodo.32932.
- Sébastien Josset, Lynn Hansen, Paola Orsolini, Michele Griffa, Olga Kuzior, Bernhard Weisse, Tanja Zimmermann, and Thomas Geiger. Microfibrillated cellulose foams obtained by a straightforward freeze–thawing–drying procedure, 2017. ISSN 1572882X.
- Jaehwan Kim, Sungryul Yun, and Zoubeida Ounaies. Discovery of cellulose as a smart material. *Macromolecules*, 39(12):4202–4206, 2006. ISSN 00249297. doi: 10.1021/ma060261e.
- Yuri Kobayashi, Tsuguyuki Saito, and Akira Isogai. Aerogels with 3D Ordered Nanofiber Skeletons of Liquid-Crystalline Nanocellulose Derivatives as Tough and Transparent Insulators. *Angewandte Chemie International Edition*, 53(39):10394–10397, jul 2014. doi: 10.1002/anie.201405123. URL <https://doi.org/10.1002/anie.201405123>.
- Todor T. Koev, Juan C. Muñoz-García, Dinu Iuga, Yaroslav Z. Khimiyak, and Frederick J. Warren. Structural heterogeneities in starch hydrogels. *Carbohydrate Polymers*, 249, 2020. ISSN 01448617. doi: 10.1016/j.carbpol.2020.116834.
- Chuxin Lei, Kai Wu, Lingyu Wu, Wenjie Liu, Rongni Du, Feng Chen, and Qiang Fu. Phase change material with anisotropically high thermal conductivity and excellent shape stability due to its robust cel-

lulose/BNNs skeleton. *J. Mater. Chem. A*, 7:19364–19373, 2019. doi: 10.1039/C9TA05067A. URL <http://dx.doi.org/10.1039/C9TA05067A>.

Tian Li, Chaoji Chen, Alexandra H Brozena, J Y Zhu, Lixian Xu, Carlos Driemeier, Jiaqi Dai, Orlando J Rojas, Akira Isogai, Lars Wågberg, and Liangbing Hu. Developing fibrillated cellulose as a sustainable technological material. *Nature*, 590(7844):47–56, 2021. ISSN 0028-0836. doi: 10.1038/s41586-020-03167-7. URL <http://dx.doi.org/10.1038/s41586-020-03167-7>. URL <http://www.nature.com/articles/s41586-020-03167-7>.

Andong Liu, Lilian Medina, and Lars A. Berglund. High-Strength Nanocomposite Aerogels of Ternary Composition: Poly(vinyl alcohol), Clay, and Cellulose Nanofibril. *ACS Applied Materials and Interfaces*, 9:6453 – 6461, 2017. doi: 10.1021/acsami.6b15561.

A. Lopez-Gil, F. Silva-Bellucci, D. Velasco, M. Ardanuy, and M. A. Rodriguez-Perez. Cellular structure and mechanical properties of starch-based foamed blocks reinforced with natural fibers and produced by microwave heating. *Industrial Crops and Products*, 66:194–205, 2015. ISSN 09266690. doi: 10.1016/j.indcrop.2014.12.025.

Aslan Miriyev and Mirko Kovač. Skills for physical artificial intelligence, 11 2020. ISSN 25225839.

Lufeng Mo, Yuan He, Yunhao Liu, Jizhong Zhao, Shao Jie Tang, Xiang Yang Li, and Guojun Dai. Canopy closure estimates with GreenOrbs: Sustainable sensing in the forest. In *Proceedings of the 7th ACM Conference on Embedded Networked Sensor Systems, SenSys 2009*, pages 99–112, 2009. ISBN 9781605587486. doi: 10.1145/1644038.1644049.

Elke Naumburg and David S. Ellsworth. Photosynthetic sunfleck utilization potential of understory saplings growing under elevated CO₂ in FACE. *Oecologia*, 122(2):163–174, 2000. ISSN 00298549. doi: 10.1007/PL00008844.

Todd A. Ontl, Maria K. Janowiak, Christopher W. Swanston, Jad Daley, Stephen Handler, Meredith Cornett, Steve Hagenbuch, Cathy Handrick, Liza McCarthy, and Nancy Patch. Forest management for carbon sequestration and climate adaptation. *Journal of Forestry*, 118(1):86–101, 2020. ISSN 19383746. doi: 10.1093/jofore/fvz062.

Alexandre Poulin, Xavier Aebly, and Gustav Nyström. Water activated disposable paper battery. *Scientific Reports*, 12(1):11919, 12 2022. ISSN 2045-2322. doi: 10.1038/s41598-022-15900-5.

Sneh Punia, Sukhvinder Purewal, Monica Trif, Sajid Maqsood, and Manoj Kumar. Functionality and Applicability of Starch-Based Films: An Eco-Friendly Approach. *Foods*, 10, 09 2021. doi: 10.3390/foods10092181.

Edna Rödiger, Matthias Cuntz, Anja Rammig, Rico Fischer, Franziska Taubert, and Andreas Huth. The importance of forest structure for carbon fluxes of the Amazon rainforest. *Environmental Research Letters*, 13(5), 2018. ISSN 17489326. doi: 10.1088/1748-9326/aabc61.

M. Roussanova, J. Enrione, P. Diaz-Calderon, A. J. Taylor, J. Ubbink, and M. A. Alam. A nanostructural investigation of glassy gelatin oligomers: Molecular organization and interactions with low molecular weight diluents. *New Journal of Physics*, 14, 2012. ISSN 13672630. doi: 10.1088/1367-2630/14/3/035016.

Houssine Sehaqui, Michaela Salajková, Qi Zhou, and Lars A. Berglund. Mechanical performance tailoring of tough ultra-high porosity foams prepared from cellulose i nanofiber suspensions. *Soft Matter*, 6(8): 1824–1832, 2010. ISSN 1744683X. doi: 10.1039/b927505c.

Houssine Sehaqui, Qi Zhou, and Lars A. Berglund. High-porosity aerogels of high specific surface area prepared from nanofibrillated cellulose (NFC). *Composites Science and Technology*, 71(13):1593–1599, 2011. ISSN 02663538. doi: 10.1016/j.compscitech.2011.07.003.

- Sarab S. Sethi, Mirko Kovac, Fabian Wiesemüller, Aslan Miriyev, and Clementine M. Boutry. Biodegradable sensors are ready to transform autonomous ecological monitoring. *Nature Ecology & Evolution*, 7 2022. ISSN 2397-334X. doi: 10.1038/s41559-022-01824-w.
- Anna J. Svagan, My A.S.Azizi Samir, and Lars A. Berglund. Biomimetic foams of high mechanical performance based on nanostructured cell walls reinforced by native cellulose nanofibrils. *Advanced Materials*, 20(7):1263–1269, 2008. ISSN 09359648. doi: 10.1002/adma.200701215.
- Anna J. Svagan, Lars A. Berglund, and Poul Jensen. Cellulose nanocomposite biopolymer foam-hierarchical structure effects on energy absorption. *ACS Applied Materials and Interfaces*, 3(5):1411–1417, 2011. ISSN 19448244. doi: 10.1021/am200183u.
- Blaise Tymen, Grégoire Vincent, Elodie A. Courtois, Julien Heurtebize, Jean Dauzat, Isabelle Marechaux, and Jérôme Chave. Quantifying micro-environmental variation in tropical rainforest understory at landscape scale by combining airborne LiDAR scanning and a sensor network. *Annals of Forest Science*, 74 (2), 2017. ISSN 1297966X. doi: 10.1007/s13595-017-0628-z.
- Chang Sheng Wang, Nick Virgilio, Paula M. Wood-Adams, and Marie Claude Heuzey. A gelation mechanism for gelatin/polysaccharide aqueous mixtures. *Food Hydrocolloids*, 79:462–472, 2018. ISSN 0268005X. doi: 10.1016/j.foodhyd.2018.01.016.
- Fabian Wiesemüller, Aslan Miriyev, and Mirko Kovac. Zero-footprint eco-robotics: A new perspective on biodegradable robots. In *IEEE AIRPHARO 2021: The 1st AIRPHARO Workshop on Aerial Robotic Systems Physically Interacting with the Environment*, pages 1–6, Biograd na Moru, Croatia, 2021. IEEE. doi: 10.1109/AIRPHARO52252.2021.9571067.
- Fabian Wiesemüller, Ziwen Meng, Yijie Hu, Andre Farinha, Yunus Govdeli, Pham H. Nguyen, Gustav Nyström, and Mirko Kovač. Transient bio-inspired gliders with embodied humidity responsive actuators for environmental sensing. *Frontiers in Robotics and AI*, 9, 10 2022. ISSN 2296-9144. doi: 10.3389/frobt.2022.1011793.
- Shanyu Zhao, Wim J. Malfait, Natalia Guerrero-Alburquerque, Matthias M. Koebel, and Gustav Nyström. Biopolymer Aerogels and Foams: Chemistry, Properties, and Applications. *Angewandte Chemie International Edition*, 57(26):7580–7608, 6 2018. ISSN 14337851. doi: 10.1002/anie.201709014.